Received: 21 January 2022 | Revised: 7 May 2022 | Accepted: 10 May 2022 | Published on: 12 June 2022

DOI: 10.1002/mrm.29318

RESEARCH ARTICLE

Magnetic Resonance in Medicine

Improved TSE imaging at ultrahigh field using nonlocalized efficiency RF shimming and acquisition modes optimized for refocused echoes (AMORE)

Xiaoxuan He | **Simon Schmidt** | **Štefan Zbýň** | **Tobey Haluptzok** | **Steen Moeller** | **Gregory J. Metzger**

Center for Magnetic Resonance Research, University of Minnesota, Minneapolis, MN

Correspondence
Gregory J. Metzger, PhD,
Center for Magnetic Resonance Research, University of Minnesota, 2021 6th Street SE, Minneapolis, MN 55455
Email: gmetzger@umn.edu

Funding information
National Institute of Biomedical Imaging and Bioengineering (NIBIB), Grant/Award Numbers: R01 EB029985, P41 EB027061; National Institutes of Health (NIH)

Purpose: To develop and evaluate a novel RF shimming optimization strategy tailored to improve the transmit efficiency in turbo spin echo imaging when performing time-interleaved acquisition of modes (TIAMO) at ultrahigh fields.
Theory and Methods: A nonlocalized efficiency shimming cost function is proposed and extended to perform TIAMO using acquisition modes optimized for refocused echoes (AMORE). The nonlocalized efficiency shimming was demonstrated in brain and knee imaging at 7 Tesla. Phantom and in vivo torso imaging studies were performed to compare the performance between AMORE and previously proposed TIAMO mode optimizations with and without localized constraints in turbo spin echo and gradient echo acquisitions.
Results: The proposed nonlocalized efficiency RF shimming produced a circularly polarized-like field with fewer signal dropouts in the brain and knee. For larger targets, AMORE was used and required a significantly lower transmitter voltage to produce a similar contrast to existing TIAMO mode design approaches for turbo spin echo as well as gradient echo acquisitions. In vivo, AMORE effectively reduced signal dropout in the interior torso while providing more uniform contrast with reduced transmit power. A local constraint further improved performance for a target region while maintaining performance in the larger FOV.
Conclusion: AMORE based on the presented nonlocalized efficiency shimming cost function demonstrated improved contrast and SNR uniformity as well as increased transmit efficiency for both gradient echo and turbo spin echo acquisitions.

KEYWORDS
MRI, parallel transmission, RF shimming, TIAMO, TSE, ultrahigh field, B1 shimming, body, head, prostate

1 | INTRODUCTION

In recent years, interest in ultrahigh field (UHF) MRI has grown due to advantages in SNR[1] and contrast,[2] along with its recent approval for clinical imaging in the head and knee. To date, clinical imaging at 7 Tesla is approved only in single transmit mode, where a transmit coil is typically operating in a default quadrature excitation or a circularly polarized (CP) mode. The challenge of B_1^+ inhomogeneity at UHF is best addressed through both parallel transmission (pTx) hardware[3,4] and RF management methods. Note that at UHF the default CP mode with pTx is typically referred to as a fixed phase distribution across transmit elements typically defined by the azimuthal positions in the array. Although a variety of strategies have been introduced to homogenize B_1^+ field such as spoke pulses,[5] k-T pulses,[6] and multi-dimensional tailored pulses,[7] RF shimming[8] remains the most generally applicable approach given its relative simplicity with respect to sequence-specific modifications and required hardware.

The issues of RF inhomogeneity and limitations in RF transmit power increase with the size of the region of interest (ROI). Therefore, an inherent tradeoff exists in RF shimming between transmit efficiency and homogeneity.[9,10] For brain and knee imaging, it is easier to achieve a more homogeneous shim with sufficient B_1^+ and acceptable specific absorption rate (SAR) given its relatively small size and volume. For body imaging, however, RF shimming is more challenging because the anatomy of interest becomes increasingly large compared to the RF wavelength and the inherent limitations in peak B_1^+ due to larger volumes being excited by the transmit coils as recently reviewed.[11,12] Empirically, even a homogeneity shim may still produce undesirable B_1^+ nulls in the torso, not to mention the relatively low transmit efficiency. Whereas an efficiency shim localized to an anatomical target of interest improves B_1^+,[10] it usually results in image nonuniformity outside the ROI (or even inside the ROI as it increases in size) compared with those acquired at standard clinical field strength. In addition, these issues are even more pronounced in turbo spin echo (TSE)–based acquisitions in the body due to increased sensitivity to low B_1^+ fields compared to gradient echo (GRE) acquisitions.[13] As a result, neither an efficiency nor a homogeneity RF shim can produce a uniform image with an optimal TSE contrast at UHF.

Methods to address competing RF shimming needs within a sequence have been previously introduced either through dynamically applying different RF pulse tailored shims within a TR[14] or through the time-interleaved acquisition of modes (TIAMO) where different RF shims or modes are employed across TRs.[15] In TIAMO, alternating complementary transmit modes between subsequent TRs can help mitigate the B_1^+ inefficiencies in either individual mode. Treating each mode as a virtual set of receive channels, a combined image can be obtained with improved uniformity at a mild cost of SNR and acquisition efficiency by undersampling each mode and using a GRAPPA[16] reconstruction. Although originally formulated using the small tip angle approximation, TIAMO has been successfully applied to TSE and B_1^+ mapping acquisitions apart from typical GRE acquisitions.[17–19]

While "standard" modes in TIAMO defined as CP and CP^{2+} often work well, especially for low flip angle GRE acquisitions, optimization of modes is possible. In terms of cost functions, it has been shown that a unity of B_1^+ in the root sum of squares of the modes can maintain T_1 weighted contrast in spoiled GRE images.[17] However, this cost function leads to a suboptimal transmit efficiency, especially impactful in TSE acquisitions in the torso, given that the solution space contains regions where neither of the modes provides the desired flip angle unless with higher transmit power. Therefore, a more efficient mode design that maintains contrast for T_2 and proton density weighted TSE acquisitions remained to be investigated and is the focus of this work.

In this study, we propose a novel nonlocalized efficiency shim combined with a novel TIAMO mode design strategy for TSE, which we referred to as *acquisition modes optimized for refocused echoes* (AMORE). The nonlocalized efficiency shim by itself is well suited for TSE imaging of smaller anatomical targets such as brain and knee, whereas AMORE provides optimized modes for TIAMO acquisitions improving TSE imaging performance in the torso by increasing B_1^+ efficiency. We present phantom and in vivo data to evaluate and compare the proposed methods to the existing optimization approaches for both TSE and GRE acquisitions. The Appendix in this paper provides a generalization of TIAMO from the small tip angle approximation to a form appropriate for TSE acquisitions to derive the necessary conditions for maintaining TSE contrast in TIAMO.

2 | THEORY

Here we briefly review efficiency cost functions in RF shimming and how they can be incorporated into the proposed TIAMO mode design. In the following context, an RF shim is synonymously referred to as a *mode*. The calculation of TIAMO modes is simply performed by calculating multiple RF shims with specific imposed constraints.

2.1 | Localized efficiency RF shimming

The goal of localized efficiency shimming is to improve B_1^+ transmit efficiency (i.e., $\mu T/W^{0.5}$) within a typically small ROI (e.g., prostate or single-voxel spectroscopy volume) and subsequently reduces total power deposition. Previous studies have introduced different metrics or cost functions to improve transmit efficiency within an ROI.[10,20] Additionally, it has been shown that localized transmit efficiency η_R can be analytically defined as the Rayleigh quotient[21,22]:

$$\eta_R = \frac{\boldsymbol{x}^H \boldsymbol{S}_R^H \boldsymbol{S}_R \boldsymbol{x}}{\boldsymbol{x}^H \boldsymbol{x}}, \tag{1}$$

where $\boldsymbol{x}$ is a $N_c \times 1$ complex vector representing shim values of a total of N_c transmit channels, and $\boldsymbol{S}_R$ is a $N_s \times N_c$ matrix of transmit sensitivities of N_c transmit channels within the specified ROI containing N_s voxels. Note that $\boldsymbol{S}_R$ is typically a subset of the transmit sensitivities in the full FOV that contains a total of N voxels (i.e., $N > N_s$), denoted as a $N \times N_c$ matrix $\boldsymbol{S}$. The above quotient represents the total B_1^+ achievable within the ROI given normalized total input power and reaches an analytical maximum $\eta_{\max}$, as given by the largest eigenvalue of the Hermitian matrix $\boldsymbol{S}_R^H \boldsymbol{S}_R$, where the corresponding eigenvector is the analytical maximum efficiency shim. In practice, such a shim may not be feasible due to hardware limitations such as per-channel power limits or a preference for a phase-only RF shim. However, it is usually a good initial guess for optimization and can serve as a quantitative metric of transmit efficiency or as an optimization constraint.

2.2 | Nonlocalized efficiency RF shimming

For nonlocalized efficiency shimming, the goal is to improve B_1^+ within the entire imaging FOV rather than a local ROI. Although the Rayleigh quotient can still be used, the resulting shim usually produces more pronounced B_1^+ inhomogeneities and undesirable B_1^+ nulls, especially with increasing target size. Such issue arises from the fact that voxels closer to coil elements typically have a higher B_1^+ and are thus weighted more in the Rayleigh quotient, unless additional constraints such as a specified minimum B_1^+[23] are imposed. In other words, the Rayleigh quotient as a cost function maximizes the total B_1^+ within a given region, which is not necessarily equivalent to minimizing B_1^+ destructive interferences. To produce a shim that is "efficient" in the sense that destructive B_1^+ interferences are minimized within the entire imaging FOV, we propose a more appropriate cost function for nonlocalized efficiency shimming that penalizes underflipping alone without explicitly constraining overflipping:

$$f(\boldsymbol{x}) = \sum_{i=1}^{N} \frac{r(|\boldsymbol{s}_i \boldsymbol{x}|)^H r(|\boldsymbol{s}_i \boldsymbol{x}|)}{\boldsymbol{x}^H \boldsymbol{x}}, \tag{2}$$

where the voxel-wise cost function is evaluated by a piecewise linear function:

$$r(\alpha) = \begin{cases} \alpha_{\min} - \alpha, & \alpha < \alpha_{\min} \\ 0, & \alpha \geq \alpha_{\min} \end{cases}. \tag{3}$$

Note that $\boldsymbol{s}_i$ are the row vectors in $\boldsymbol{S}$; $\alpha = |\boldsymbol{s}_i \boldsymbol{x}|$ is the magnitude of voxel-wise B_1^+ under the given shim $\boldsymbol{x}$; and $\alpha_{\min}$ is the threshold for minimum B_1^+ magnitude to be used during optimization. When $\alpha_{\min}$ is large enough, the above cost function will approach the Rayleigh quotient and thus produce similar solutions.

2.3 | AMORE cost function

Whereas different B_1^+ modes in TIAMO are treated as virtual receive channels during reconstruction, a significant distinction from physical receive channels is that the underlying magnetization is impacted by the modes, thus influencing image contrast in addition to SNR. To date, TIAMO has been described using the small tip angle approximation and is later optimized for T_1 weighted GRE acquisitions.[17] We have derived an analysis to explain how multiple modes can be optimized to maintain contrast in TSE acquisitions (see Appendix). In summary, it is demonstrated that for proton density or T_2 weighted TSE at least 1 of the modes must achieve the target flip angle in order to produce the desired contrast in the final reconstructed images. To generate modes appropriate for maintaining performance (i.e., contrast and SNR) for TSE imaging, we extend the nonlocalized efficiency shimming cost function to include multiple transmit modes while requiring at least 1 of the modes to achieve the nominal flip angle. Thus, we propose the following AMORE cost function:

$$f(\boldsymbol{x}) = \sum_{i=1}^{N} \frac{r(\alpha_M)^H r(\alpha_M)}{\boldsymbol{x}_M^H \boldsymbol{x}_M}, \tag{4}$$

where $\alpha_M = \max_{m \in \{1,2,\ldots,N_m\}} |\boldsymbol{s}_i \boldsymbol{x}_m|$ is the voxel-wise maximum flip angle across a total of N_m transmit modes. In cases where a tradeoff between efficiency and homogeneity is needed, the voxel-wise cost function can

be adapted to:

$$r(\alpha) = \begin{cases} \alpha_{\min} - \alpha, & \alpha < \alpha_{\min} \\ 0, & \alpha_{\min} \le \alpha \le \alpha_{\max} \\ \alpha - \alpha_{\max}, & \alpha > \alpha_{\max} \end{cases}, \quad (5)$$

where $\alpha_{\min}$ and $\alpha_{\max}$ are the tunning parameters for the tolerance levels of B_1^+ inhomogeneities.

3 | METHODS

3.1 | Design considerations

Compared with RF shimming, TIAMO affords more degrees of freedom for optimization to satisfy certain constraints, including peak local SAR. To further exploit these advantages, we propose the option of a new TIAMO implementation that incorporates an efficiency constraint within a specified local ROI. The motivation is to combine the advantages of both local RF shimming and TIAMO, namely, to maintain a relatively high transmit efficiency in a specified target (e.g., in prostate where the peak B_1^+ is often a limiting factor) while generating complementary modes to improve overall image quality. In the following context, we refer this local efficiency constrained implementation as *localized* to differentiate from the typical *nonlocalized* TIAMO.

Both localized and nonlocalized versions of TIAMO are explored comparing the previous least squares (LS) optimization of modes[17] in comparison to AMORE described above. In addition to minimizing the cost functions (i.e., LS or AMORE), as is the case with nonlocalized TIAMO, the design of localized TIAMO imposes an additional constraint on the first mode to satisfy $\eta_R \ge Q \cdot \eta_{\max}$, as characterized by Equation [1], where $0 < Q < 1$ is a specified efficiency quality factor evaluated within the ROI. With appropriate solvers, this allows a trade-off between the minimum transmit efficiency in a local ROI and mode complementariness. Additional constraints can also be incorporated into the design, such as local SAR constraints when a set of virtual observation points (VOP) is defined for a given coil.[24] The shim or mode solutions correspond to the minima of the cost functions in Equations [2] and [4]. Dependent on whether or not constraints are imposed, mode optimization will be a constrained or unconstrained nonlinear minimization problem, which can be solved by a variety of algorithms such as interior-point method (constrained) or quasi-Newton method (unconstrained).

The choice of $\alpha_{\min}$ is implemented as a tuning parameter in the sequence user interface, where its value is determined by a user-specified percentile of the default CP mode B_1^+ distribution. Empirically, $\alpha_{\min}$ is set to the 50th percentile for nonlocalized efficiency shimming in smaller anatomies and the 75th percentile for AMORE design in larger anatomies. Regarding the local minima problems in Equation [2], we empirically observed that phase-only optimizations converged well with a default CP mode as the initial guess, producing a CP-like shim with significantly reduced B_1^+ nulls. For phase-magnitude optimizations, we implemented a 2-step approach, namely, solving initially a phase-only optimization followed by a phase-magnitude optimization for demonstrating the potential of AMORE to reduce peak local SAR. The appropriate method of local SAR supervision is often dependent on the RF shimming method employed. For phase-only solutions, per-channel power limits are sufficient. However, when employing phase-magnitude solutions, it is more appropriate to use VOPs to avoid being too restrictive with total power deposition. Because VOPs have not yet been implemented for the RF coil used at 7 T, phase-only solutions were used for all experimental studies, whereas phase-magnitude solutions were explored with simulation data.

3.2 | MRI system

All imaging experiments were performed on a Siemens Magnetom 7 Tesla MRI scanner (Siemens Healthcare, Erlangen, Germany) with a whole-body gradient system and a full 16×1 kW pTx system. TIAMO was implemented in the GRE and TSE sequences, and the modes were calculated online by a customized MATLAB (R2012b, MathWorks, Natick, MA) plugin interfaced to the sequence. Per-channel B_1^+ maps needed for mode optimization in brain/pelvis were acquired using the presaturated turbo-FLASH[25] sequence with FOV = $256 \times 256/500 \times 500\,\text{mm}^2$, matrix size = $64 \times 64/128 \times 128$, and acquisition time = 01:16 min (8-channel transmit) and 01:38 min (16-channel transmit). In vivo imaging was conducted under an institutional review board-approved protocol for which all subjects provided signed written consent before participating. The local SAR was supervised using the per-channel power limit approach based on SAR limits defined by the International Electrotechnical Commission guidelines. As such, phase-only solutions were used for all MRI experiments.

3.3 | In vivo RF shimming study

To illustrate the properties of the nonlocalized efficiency cost function, in vivo studies in smaller anatomic targets

were performed. A transverse 2D, multi-slice T_2w TSE brain acquisition using the proposed nonlocalized efficiency shimming was acquired in 2 subjects and compared to the CP mode acquisition with an 8-channel transmit 32-channel receive head coil (Nova Medical, Wilmington, MA). In the knee, a sagittal proton density weighted TSE acquisition was performed in 1 subject using a home-built 16-channel transmission line transceiver array, where all elements are distributed around a circle in the axial plane with each spanning the whole length of the coil in the z direction.[26] The acquisition parameters for both studies are shown in Table 1.

All RF shim calculations (phase-only) were performed using multi-slice B_1^+ calibration data. To demonstrate the improvements of the proposed shim, the predicted B_1^+ maps along with the mean, root mean square (RMS), and 2.5th and 97.5th percentiles of the B_1^+ histogram were calculated. To help illustrate the signal variation in the TSE images due to B_1^+ inhomogeneity, the predicted TSE signal map was simulated using the measured B_1^+ maps and protocol parameters for the brain acquisitions.

3.4 | Phantom AMORE study

To evaluate the contrast uniformity of different TIAMO mode optimizations, a custom phantom was developed to support the quantitative evaluation of spatial contrast performance across a large FOV. A total of 101 15 mL falcon tubes were submerged in a ~ 50% polyvinylpyrrolidone weight/volume slurry with electrical properties close to those in the human body with a relative permittivity of 51 and conductivity 0.58 S/m. All tubes were filled with 1 of the 2 solutions (17 mM NiCl, 0.031 mM $MnCl_2$) to provide both T_1 and T_2 contrast with values representative of human tissues.

Two-mode nonlocalized phase-only solutions were calculated using the previously introduced least-squares cost function (referred to as LS-TIAMO)[17] and the AMORE cost function. Both GRE and TSE TIAMO imaging were performed using a 16-channel loop-dipole transceiver array at 7 Tesla[27] with the acquisition parameters shown in Table 1. As a reference, a separate acquisition with CP mode and nonlocalized efficiency shimming was performed to demonstrate B_1^+ inhomogeneities and the performance of static RF shimming.

To evaluate the performance of different design approaches, the contrast-to-noise ratio (CNR) was calculated and defined as: $\mathrm{CNR} = \frac{|S_{tube} - S_{pvp}|}{\sigma}$, where S_{tube} and S_{pvp} are the mean signal intensities of a given tube and its surrounding PVP, respectively. The noise level is calculated as $\sigma = g \cdot \sqrt{R} \cdot SF \cdot \sigma_{FID}$, in which g is the g-factor from GRAPPA reconstruction; R is the acceleration factor; *SF* is the scaling factor to map noise from k-space to image space; and σ_{FID} is the SD of the FID noise scan.

The complex k-space data were first decorrelated using the measured noise covariance matrix before performing the GRAPPA reconstruction to obtain mode-combined TIAMO images. A MATLAB (R2019b, MathWorks) script was written to automate the extraction of the tubes from images and generate masks for both tubes and their surrounding PVP, which were visually inspected before being used to calculate CNR.

3.5 | In vivo AMORE study

A total of 5 male volunteers were recruited and participated in imaging studies of the pelvis to explore the nonlocalized and localized TIAMO design approaches focusing on the prostate and surrounding anatomy. The same 16-channel loop-dipole array was used for imaging. As a reference, a transverse 2D T_2w TSE acquisition with a localized efficiency phase shimming targeted to the prostate was performed to determine the transmitter voltage that would be used throughout the acquisitions as well as to provide a reference contrast in the prostate.[7] For each subject, 2-mode phase-only TIAMO TSE acquisitions were performed with a subset, or all, of the following designs: (1) nonlocalized LS-TIAMO, (2) nonlocalized AMORE, (3) localized LS-TIAMO ($Q \geq 0.85$ for η_{max} in the prostate), (4) localized AMORE ($Q \geq 0.85$ for η_{max} in the prostate), and (5) standard TIAMO (CP and CP^{2+}). The acquisition parameters are shown in Table 1. The maps of maximum B_1^+ across all modes were calculated for each design, where the B_1^+ distribution by percentile in standard TIAMO was used as the reference to demonstrate the difference between mode strategies.

To demonstrate the performance of full phase-magnitude optimization, an additional calculation was performed using the field maps from the electromagnetic simulation of the coil with the virtual human model Fats29 (Sim4Life; Zurich Medtech, Zurich, Switzerland). To perform this optimization, VOPs were generated from the Q-matrices and used in the optimization to constrain the local SAR for nonlocalized LS-TIAMO and AMORE not to exceed 80% of that realized with standard TIAMO. The SAR efficiency defined as median B_1^+ divided by the square root of peak local SAR is used to compare the transmit efficiency among different mode designs.

TABLE 1 Acquisition parameters of phantom and in vivo imaging studies

Study	Target	Sequence	TR/TE (ms)	FA (deg)	FOV (mm^2)	Slices	Resolution (mm^3)	AF	TF	ESP (ms)	BW (Hz)	TA (min)
In vivo RF shimming	Brain	2D axial T_2w TSE	8000/62	130	256 × 256	24	1 × 1 × 3	1	12	8.84	287	03:06
	Knee	2D sagittal PDw TSE	2500/30	130	140 × 140	31	0.35 × 0.41 × 2.5	1	7	9.92	568	05:12
Phantom AMORE	Phantom	2D axial T_2w TSE	7000/68	120	225 × 450	16	1 × 1 × 3	1	13	8.48	485	02:08
		2D axial T_2w TSE (TIAMO)	7000/68	120	225 × 450	16	1 × 1 × 3	2	13	8.48	485	02:36
		2D axial T_1w GRE	7.5/2.81	25	225 × 450	16	1 × 1 × 3	1	N/A	N/A	490	00:28
		2D axial T_1w GRE (TIAMO)	7.5/2.81	25	225 × 450	16	1 × 1 × 3	2	N/A	N/A	490	00:31
In vivo AMORE	Pelvis	2D axial T_2w TSE	7000/65	120	465 × 465	16	0.69 × 0.69 × 3	1	13	9.22	392	06:06
		2D axial T_2w TSE (TIAMO)	7000/65	120	465 × 465	16	0.69 × 0.69 × 3	2	13	9.22	392	06:34

Note: AF, acceleration factor; AMORE, acquisition modes optimized for refocused echoes; TF, turbo factor; BW, bandwidth (per pixel); ESP, echo spacing; FA, flip angle; GRE, gradient echo; N/A, not applicable; PDW, proton density weighted; TA, time of acquisition; TIAMO, time-interleaved acquisition of modes; TSE, turbo spin echo.

4 | RESULTS

4.1 | In vivo RF shimming study

For the brain imaging study, the proposed nonlocalized efficiency shimming significantly reduced areas with low B_1^+ and field asymmetries. By comparison, the default CP mode suffered from subject-specific B_1^+ inhomogeneity patterns, which degrade image contrast (Figure 1). The proposed shim maintained a "CP-like" field for both subjects (Figure 2), while increasing B_1^+ at the 2.5th percentile in the presented slice by approximately 34% and 12% in subjects 1 and 2, respectively. The B_1^+ at the 97.5th percentile remained approximately the same (i.e., increased by 2% and −2% in the 2 subjects). The predicted TSE signal map matched the acquired images and demonstrated reduced signal dropout with the proposed shim.

For the sagittal knee imaging study, the proposed shimming improved overall B_1^+ efficiency in addition to reducing areas of low B_1^+ (Supporting Information Figure S1). The B_1^+ at the 2.5th and 97.5th percentiles in the presented slice was increased by approximately 25% and 15%, respectively. Note that there are less degrees of freedom for RF shimming in the sagittal plane than in the axial plane due to the design of the knee coil.

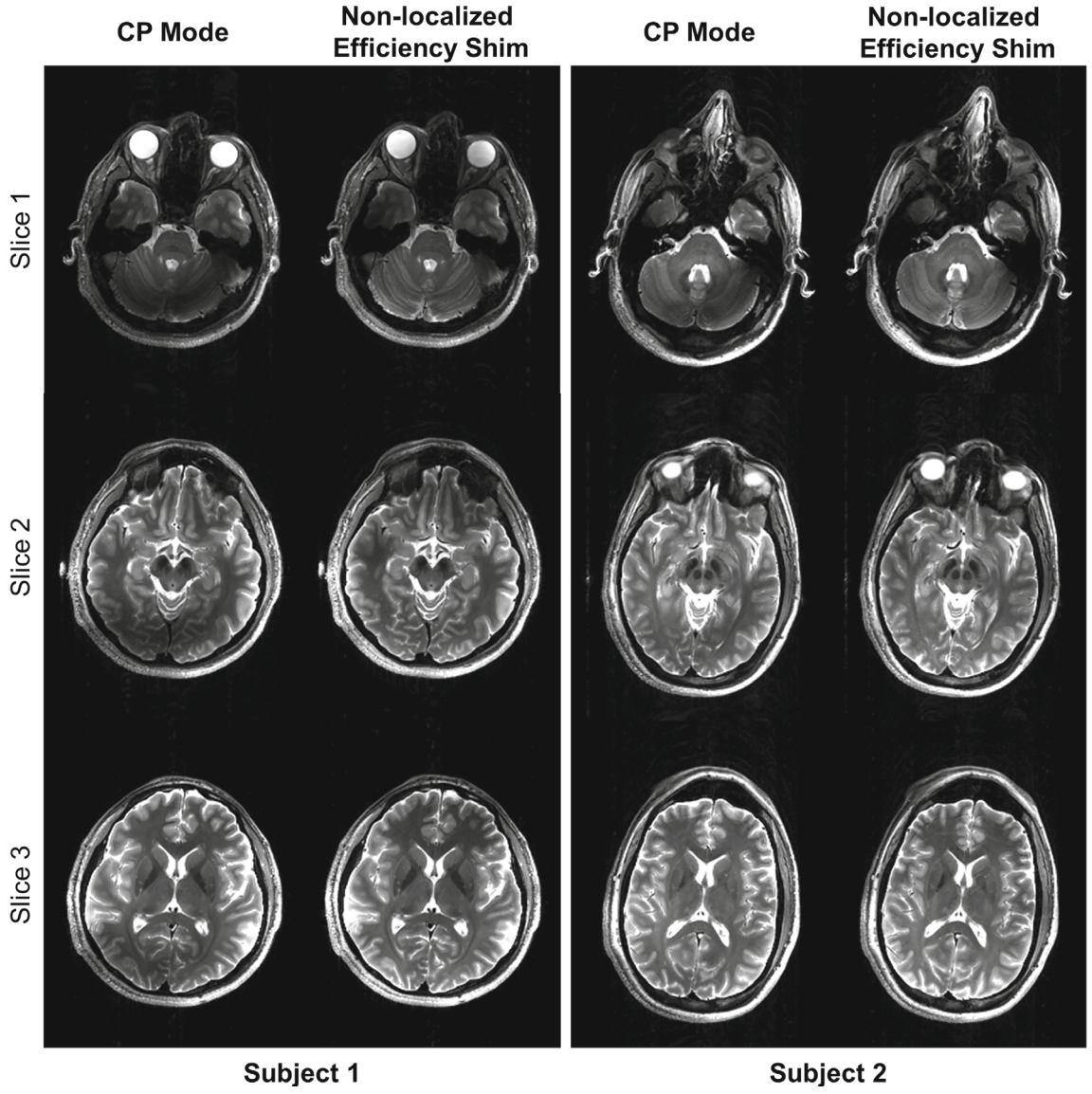

FIGURE 1 Several slices from T_2w TSE acquisitions are shown in the human brain of 2 subjects with the default CP mode and the proposed nonlocalized efficiency shim. The default CP mode produced subject-specific shading in the images, such as in the cerebellum in both subjects and the posterior cortex primarily in subject 1. In both cases, this shading was mitigated by using the subject-specific nonlocalized efficiency shimming. Both the default CP mode and the proposed shim used the same transmitter voltage for image acquisition. CP, circularly polarized; TSE, turbo spin echo.

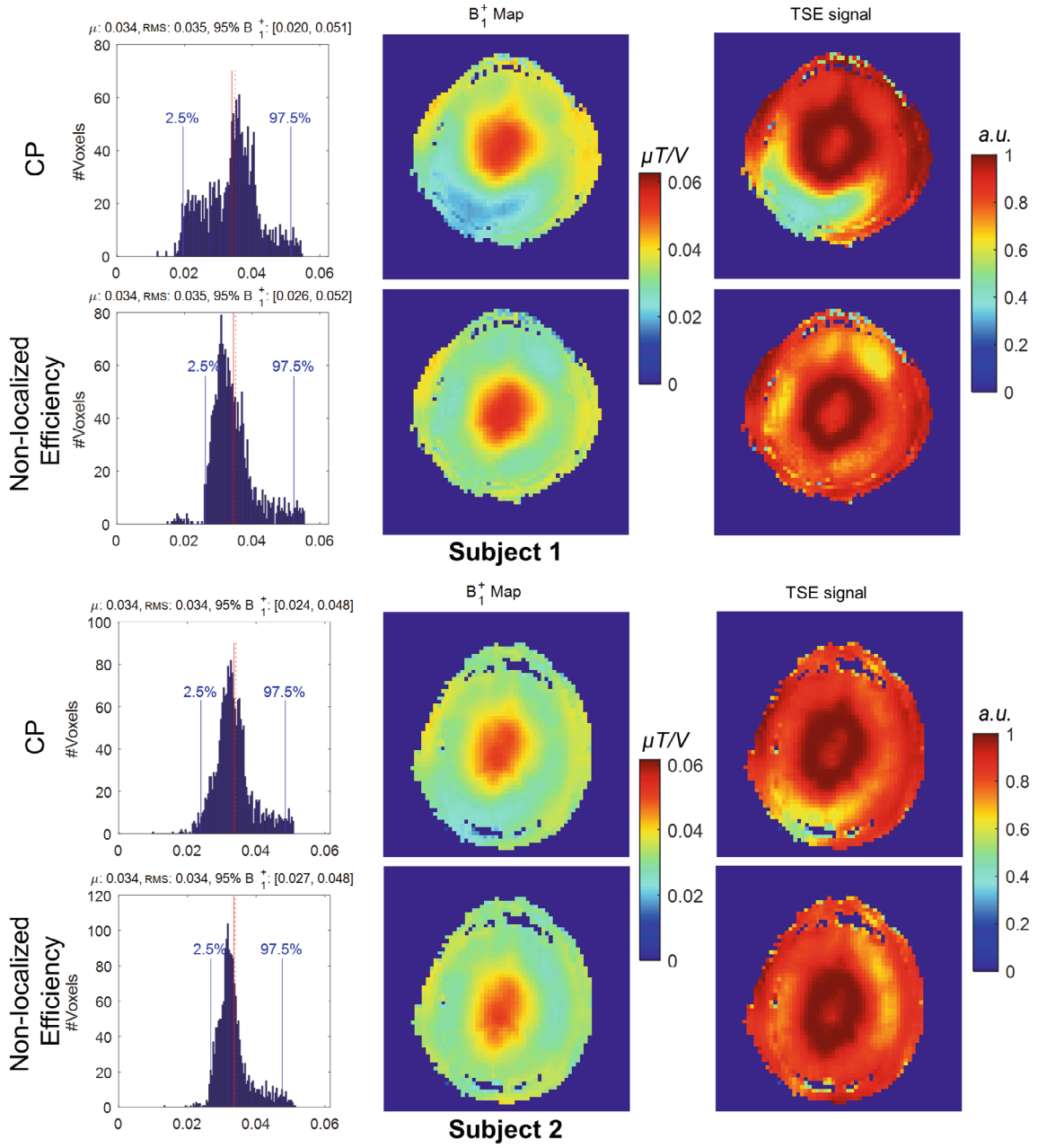

FIGURE 2 Comparisons of the default CP mode and proposed nonlocalized efficiency shim in the in vivo brain imaging studies of the 2 subjects, as illustrated by the histograms of voxel-wise B_1^+, predicted B_1^+ maps, and predicted TSE signal maps based on the acquired calibration data. The proposed shimming strategy maintains areas of high B_1^+ while reducing regions of low B_1^+ present in the default CP mode. μ, mean value (red solid line); a.u.: arbitrary unit; RMS, root mean square (red dashed line).

These examples demonstrate the characteristics of the nonlocalized efficiency shimming, namely, minimizing underflipping while not explicitly constraining overflipping.

4.2 | Phantom AMORE study

The reconstructed T_1w GRE and T_2w TSE acquisitions are shown in Figure 3. Compared with CP mode, the nonlocalized efficiency shim reduced signal dropout in both GRE and TSE acquisition, although to a lesser extent in the latter. For GRE acquisitions, both LS-TIAMO and AMORE demonstrated improved uniformity without any noticeable signal dropout when compared with the static RF shimmed acquisitions. For T2w TSE acquisitions, however, LS-TIAMO suffers from more pronounced shading than AMORE, unless acquired with a higher transmitter voltage. For both T1w GRE and T2w TSE images, AMORE produced a similar visual contrast and

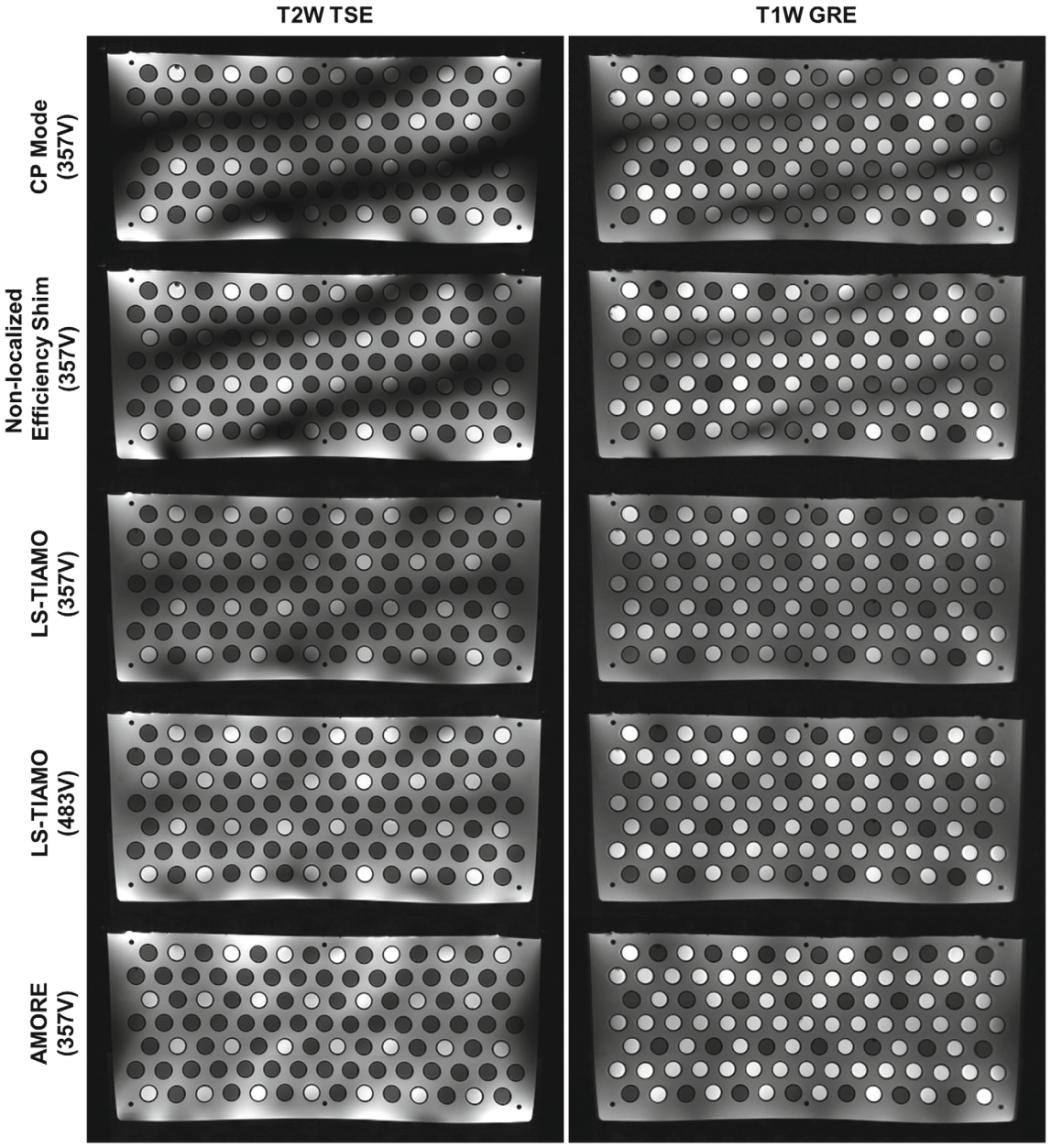

FIGURE 3 Comparison of T_2w TSE (left) and T_1w GRE images (right) acquired using CP mode, nonlocalized efficiency shim, LS-TIAMO, and AMORE. TSE acquisition is more sensitive to low B_1^+ than GRE acquisition, as shown by the images acquired with CP and nonlocalized efficiency shim, although the latter reduced signal dropout in both acquisitions. Overall better improvements are achieved when using TIAMO. Compared to the LS-TIAMO acquisition acquired at a reference voltage of 357 V, AMORE exhibits reduced B_1^+ nulls and higher, more uniform contrast in the T_2w images at the same driving voltage (lower row). In order to obtain a similar contrast and uniformity as with AMORE, the LS-TIAMO modes need to be driven with 35% higher voltage (i.e., 483 V), which is 82% more power. Whereas AMORE is designed and optimized for TSE-based contrasts, the increased transmit efficiency and uniformity across modes clearly benefit other types of acquisitions, as evidenced by comparing the performance of the T_1w GRE images (right column), where advantages similar to the T_2w comparison can be observed. AMORE, acquisition modes optimized for refocused echoes; GRE, gradient echo; LS-TIAMO, least squares–time-interleaved acquisition of modes.

CNR (Figure 4C, 4D)to LS-TIAMO at a lower transmitter voltage. Based on the maximum of B_1^+ maps across modes, AMORE improves mean B_1^+ by 35% (Figure 4A, 4B) at a mild cost of increased nonuniformities, most notably on the far left and right sides of the phantom.

4.3 | In vivo AMORE study

An example dataset of in vivo TSE acquisitions in the torso is provided in Figure 5. AMORE greatly reduced signal dropouts in the interior torso and produced an overall higher contrast with the least overall B_1^+ shading

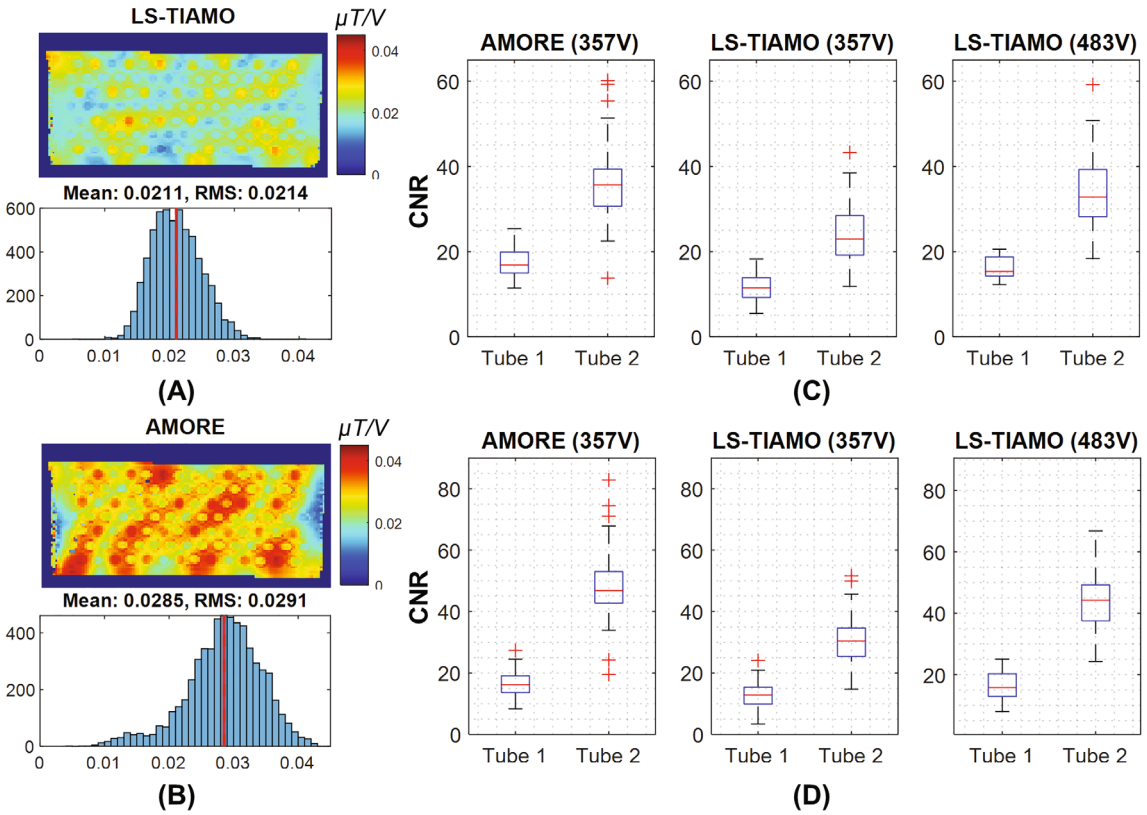

FIGURE 4 Phantom B_1^+ and CNR evaluation: the B_1^+ maps (maximum across modes) for LS-TIAMO (A) and AMORE (B) are shown along with their corresponding histograms. AMORE provides a mean B_1^+ increase of 35%, as indicated by the difference in the solid red line in the histograms shown in (A) and (B). The CNRs of the T_1w GRE (C) and T_2w TSE (D) were calculated for all tubes in the images acquired with different TIAMO approaches, where AMORE achieved improved CNR compared to LS-TIAMO acquired at the same transmit voltage of 357 V. With LS-TIAMO acquired at the higher transmit voltage of 483 V, a similar CNR ratio was obtained compared to AMORE, albeit with a slightly lower variability due to the presence of outliers in the AMORE acquisition originating from a limited number of vials at the phantom's boarder (red crosses). The tube group 1 has a total of 73 tubes, and the tube group 2 has a total of 28 tubes. The boxplot is characterized by a standardized 5-number summary including minimum, 25th percentile, median, 75th percentile, and maximum CNR values. CNR, contrast-to-noise ratio.

compared with other mode design approaches. Both nonlocalized (Figure 5A) and localized AMORE (Figure 5B) appeared similar and maintained the desired contrast in the prostate when compared with the locally shimmed (i.e., single mode) TSE acquisitions (Figure 5B), while greatly improving image quality throughout the rest of the pelvis. The localized LS-TIAMO showed improvements most notably in the prostate compared to the nonlocalized LS-TIAMO, but residual shading and signal dropout remained in the neurovascular bundles around the prostate as well as in the femoral heads. The B_1^+ maps (maximum across modes) of the different design strategies are shown in Figure 6, where the low B_1^+ areas well matched the shading in the final combined images, demonstrating the necessity of optimizing for maximum flip angle across all modes for TSE acquisitions.

The mean of B_1^+ improvement by percentile compared with standard TIAMO across all subjects was calculated and shown in Figure 6B, demonstrating an overall higher B_1^+ when using the AMORE design. To characterize the subject-specific variability of these improvements, bar plots with error bars (mean ± SD) were shown in Figure 6C for a set of representative locations, namely, the 2.5th, 25th, 50th, 75th, and 97.5th percentiles. The greatest improvements were from low B_1^+ areas where the mean B_1^+ at the 2.5th percentile was increased by 89% and 91% for nonlocalized and localized AMORE, respectively. Improvements at the 2.5th percentile were limited to 30% and 44% for nonlocalized and localized LS-TIAMO. At the 97.5th percentile, the mean B_1^+ was increased by 5% and 12% for nonlocalized and localized AMORE, respectively, and −31% and −14% for nonlocalized and localized LS-TIAMO, respectively. The positive vertical offset of the AMORE solutions across the entire B_1^+ distribution in Figure 6B demonstrates an overall increase in transmit efficiency, which contributes to the improved CNR of the AMORE acquisitions.

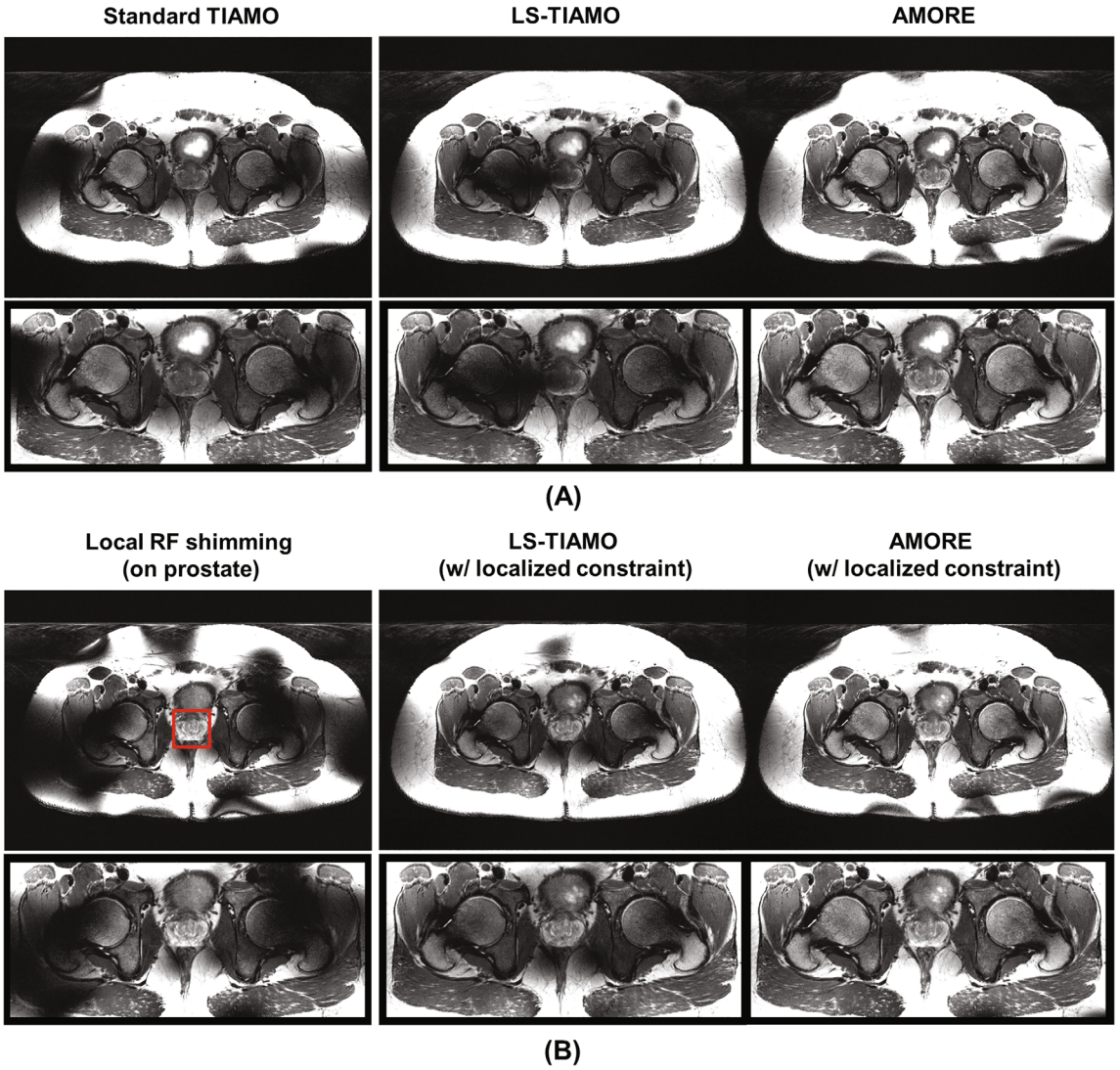

FIGURE 5 A single subject's T_2w TSE dataset of the pelvis where full FOV and zoomed-in images are shown for all experimentally tested strategies both with and without local constraints. For those without local constraints (A), standard TIAMO with default CP and CP^{2+} modes (left), nonlocalized LS-TIAMO (middle), and nonlocalized AMORE (right) are shown. For those with local constraints using an ROI (red square box) targeting the prostate (B), a single mode localized efficiency shim (left), localized LS-TIAMO (middle), and localized AMORE (right) are shown. Improvements over existing local RF shimming and nonlocalized LS-TIAMO methods are demonstrated with LS-TIAMO using local constraints and AMORE as characterized by reduced B_1^+ shading and overall higher signal in the interior torso (e.g., neurovascular bundles, rectum, obturator muscles, femoral heads), all while maintaining the desired T_2w contrast and signal intensity in the prostate using the localized RF shimming results as a reference (i.e., left most example in B). For AMORE, a mild overflipping was observed near the coil elements, resulting in a shading observed in the subcutaneous lipid.

To demonstrate the robustness of AMORE to different torso shapes and sizes, additional in vivo datasets are provided in Figure 7 (zoomed-in versions) and Supporting Information Figure S2, respectively. In general, AMORE consistently produced higher signal intensities and contrast uniformity in the interior torso with the presence of increased overflipping near coil elements, resulting in nonuniformities mostly in the subcutaneous fat. Compared with standard TIAMO and nonlocalized LS-TIAMO, the nonlocalized AMORE consistently produced a better contrast in the prostate that is closer to the locally shimmed acquisitions used as a reference (Figure 7). The robustness of AMORE is also highlighted by subject 4, where the local RF shimming failed in the prostate due to an incorrect placement of the shimming volume. In this case, both the localized and nonlocalized AMORE produced the desired contrast in the prostate in comparison to LS-TIAMO. In fact, the localized AMORE was shown to be tolerant of this misplacement, whereas the localized LS-TIAMO suffered from

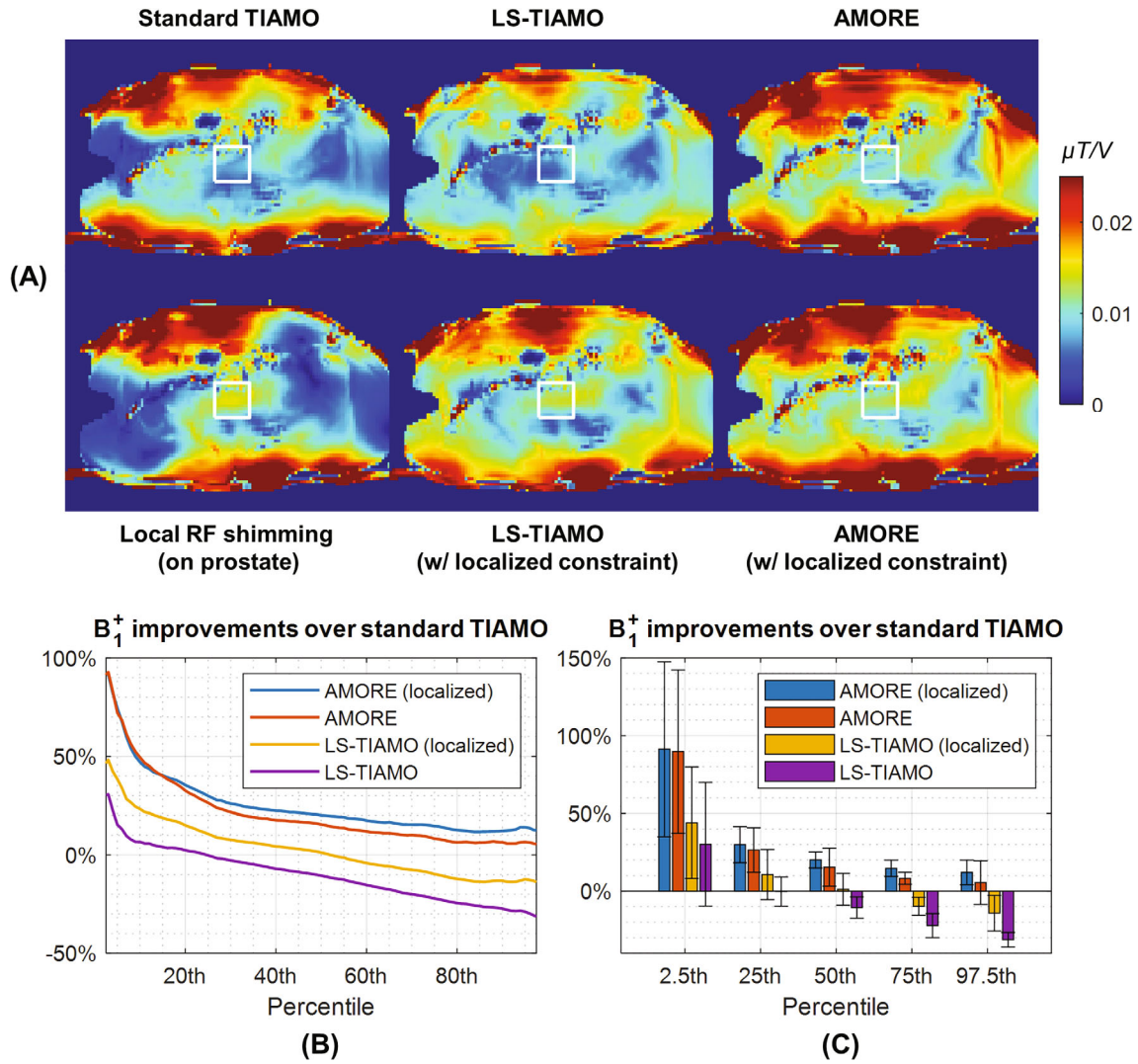

FIGURE 6 (A) The B_1^+ maps (maximum across all modes) from the 6 RF shimming and TIAMO strategies shown in Figure 5. The local RF shimming (single mode) strategy (lower left in A) improved B_1^+ in the prostate (white square box) the most but introduced largely varying B_1^+ fields outside the prostate. When using standard TIAMO and both localized and nonlocalized LS-TIAMO, varying levels of improvements were achieved; however, residual areas of low B_1^+ remained. In contrast, both nonlocalized and localized AMORE produced a more uniform B_1^+ field in the interior of the torso while maintaining the B_1^+ in the prostate. The mean of B_1^+ improvement by percentile in the full FOV compared to standard TIAMO across all 5 subjects are shown in (B), demonstrating the overall highest B_1^+ improvements when using AMORE. To characterize subject-specific variability of the improvements in (B), bar plots with errors (mean +/− SD) are provided in (C) for a set of representative percentiles, demonstrating that AMORE improves low B_1^+ areas (low percentiles) while not significantly reducing high B_1^+ (high percentiles).

residual shading in the posterior prostate and rectal wall (Figure 7).

For the phase-magnitude optimization using the simulated field maps from the virtual human model Fats29, the maximum B_1^+ maps and voxel-wise histograms of different solutions are shown in Figure 8. Both LS-TIAMO and AMORE solutions satisfied the desired local SAR constraint. When compared against the CP mode, the relative peak local SAR values for TIAMO, LS-TIAMO, and AMORE were 61%, 48%, and 48%, respectively, whereas the relative SAR efficiencies were 153%, 136%, and 200%, respectively. These results demonstrate that the highest gains in transmit and SAR efficiency were achieved with AMORE.

5 | DISCUSSION

In this study, we proposed a new cost function for nonlocalized efficiency shimming and extended it to AMORE to improve TSE acquisitions at UHF. The proposed cost function underlying this approach is inspired by the

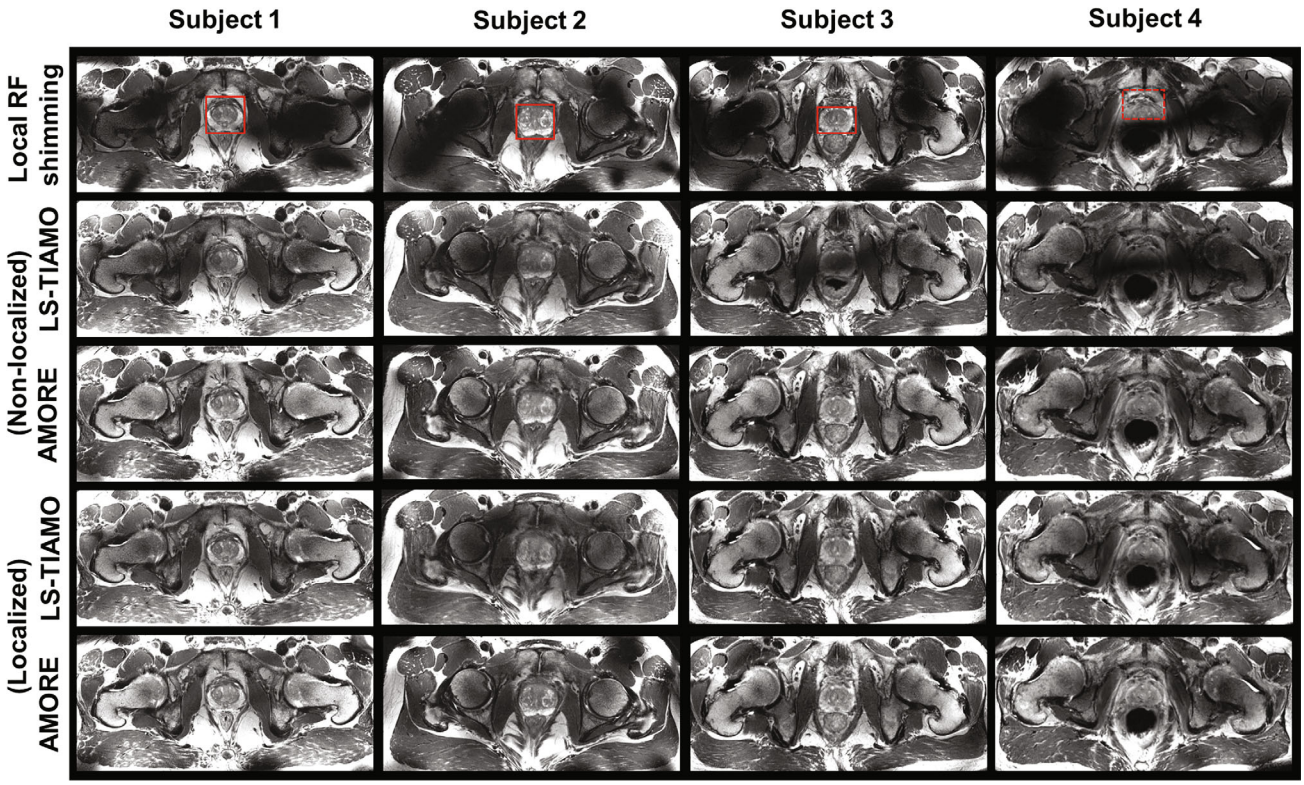

FIGURE 7 Zoomed-in versions of the in vivo T_2w TSE torso images acquired in 4 subjects using local RF shimming, LS-TIAMO, and AMORE (both with nonlocalized and localized approaches), highlighting the region of greatest radiological interest. The local ROIs were depicted by the red square boxes in the static RF shimmed acquisition, which were also used in the localized LS-TIAMO and AMORE. The nonlocalized and localized AMORE overall looked similar, and both resulted in a more uniform interior torso as well as a better contrast in the prostate that approaches the locally shimmed acquisitions. The nonlocalized LS-TIAMO resulted in most pronounced shading in the interior torso and can be improved by the proposed localized design. However, such improvements are subject-specific and can be impacted by the misplacement of shimming volume, as is the case with subject 4, where the misplaced shimming volume (red dashed box) resulted in a failed locally shimmed acquisition and localized LS-TIAMO, as indicated by the shading in the posterior prostate and its adjacent rectum walls. With either nonlocalized or localized AMORE approach, 2 phase-only modes appeared sufficient to effectively reduce signal dropout in the interior torso.

observation that the contrast in TSE images is impacted to a greater extent by underflipping than overflipping. Our results demonstrate that the nonlocalized efficiency RF shimming and AMORE can be used in different anatomies to minimize areas with low B_1^+ and thus reduce signal dropout and/or increase transmit efficiency even with phase-only modes.

As demonstrated in the brain, the proposed nonlocalized efficiency shimming can be used to produce a CP-like field pattern with less subject-specific imperfections. For torso imaging, our phantom results demonstrated a similar improvement in GRE acquisitions, although it may still be inadequate for TSE acquisitions. When using AMORE instead, greater improvements can be achieved featuring overall higher B_1^+, reduced signal dropouts, and better contrast in the interior torso while outperforming existing TIAMO design approaches. By including the proposed local constraint, both LS-TIAMO and AMORE benefit local targets while simultaneously maintaining reasonable contrast in larger FOVs, with localized AMORE presenting the best compromise between target anatomy contrast and overall performance in the rest of the imaging FOV. Note that our in vivo multi-slice T_2w TSE acquisitions in the pelvis used hyper-echoes (TRAPS, transition into static pseudo steady state)[28] to reduce SAR deposition, which is implemented as a modulation of the flip angle in the refocusing pulse train and may also be used in the 3D TSE acquisition.[29] It is therefore expected that AMORE can also work for 3D T_2w TSE acquisitions while maintaining the contrast.

Compared with LS optimization for TIAMO, AMORE minimizes B_1^+ nulls by directly penalizing underflipping without explicitly penalizing overflipping. As a result, the B_1^+ in the interior torso was improved at a mild cost of increased overflipping near the transmit coil elements. Such overflipping is partly due to the field inhomogeneities of the loop elements that we used in the study, which are inherently decoupled from dipole elements and

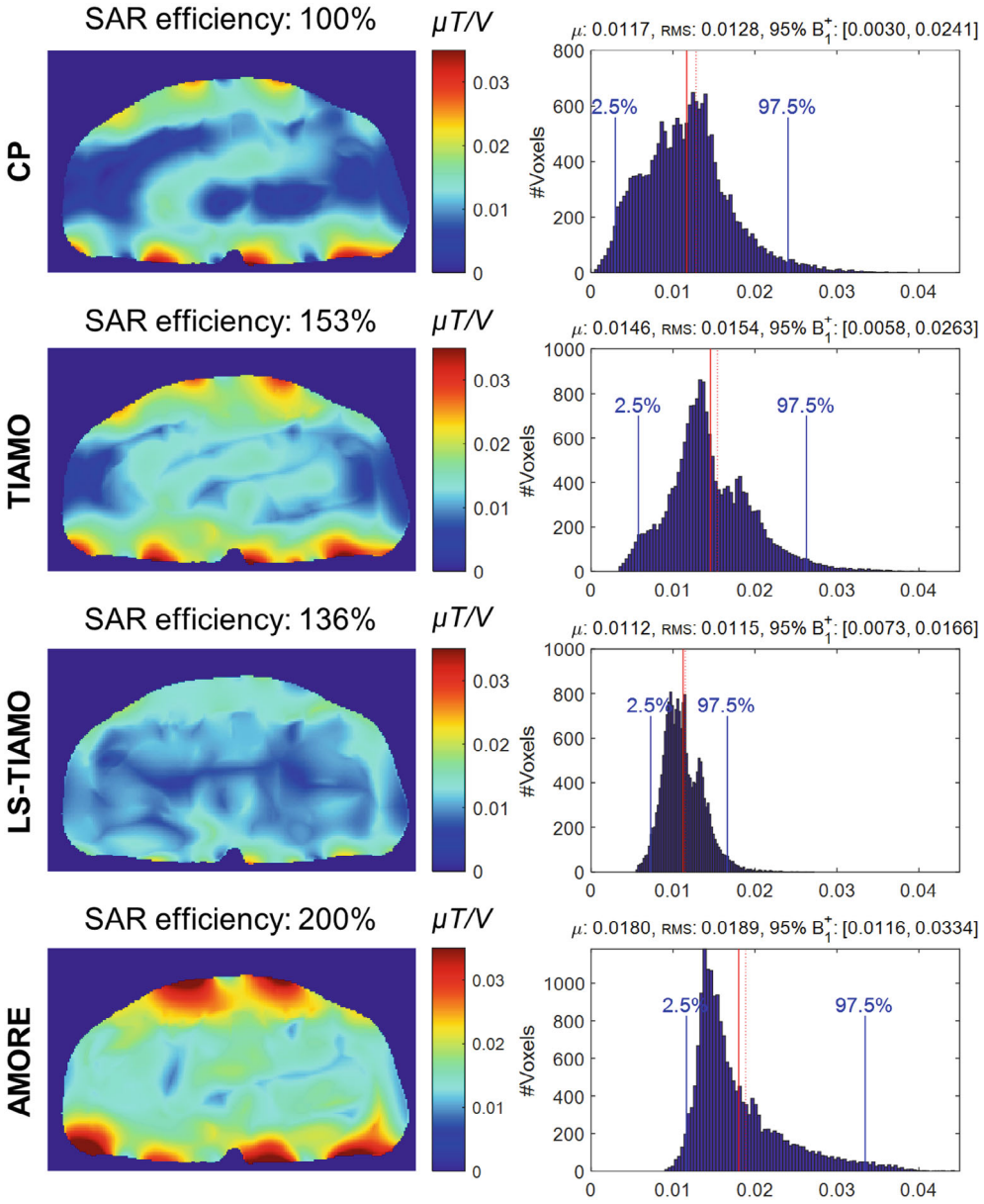

FIGURE 8 Demonstration of increased SAR efficiency using AMORE optimized with SAR constraints. Shown are the comparison of B_1^+ maps (maximum across modes) and the voxel-wise histograms with summary statistics for the CP mode, standard TIAMO, and SAR constrained versions of LS-TIAMO and AMORE calculated using the EM simulated field maps of the coil with Fats29. Both LS-TIAMO and AMORE were nonlocalized solutions using phase-magnitude optimization with a peak local SAR constraint of no more than 80% of that obtained with standard TIAMO. Driven by a combination of reduced peak local SAR and increased transmit efficiency, AMORE achieved the greatest SAR efficiency while minimizing areas with low B_1^+.

therefore effectively increase element density to increase B_1^+ and SAR efficiency at 7 T.[27]

One disadvantage of TIAMO compared to standard static RF shimming is the SNR penalty resulting from the use of parallel imaging to maintain a nearly equivalent scan time compared to non-TIAMO acquisitions. This results in a more pronounced noise amplification, especially for highly accelerated acquisitions. Such SNR penalties can be mitigated by either using RF coils with more receive channels[30,31] or alternative reconstruction methods such as ESPIRiT,[32] RAKI,[33] and supervised or self-supervised deep learning–based approaches.[34–38] As demonstrated in the Appendix, the combined TIAMO images remain weighted by a B_1^+-dominated term in addition to the receive sensitivity. Given that neither LS-TIAMO nor AMORE is explicitly optimized for the uniformity of this term, the resulting images may still manifest a subtle spatially nonuniform weighting, which may be ameliorated by using N4 ITK[39] and UNICORN.[40]

Although body imaging at UHF, especially TSE imaging, is challenging due to inhomogeneities and limited peak B_1^+, our results demonstrate that the B_1^+ shading and nulls in the torso can be effectively reduced by designing 2 phase-only modes with AMORE. The concept is extended in a straightforward manner to more modes as might be beneficial with increasing field strength such as 10.5 T, where the benefits and limitations of static RF shimming have been previously demonstrated.[41–43] Further improvements are possible by using phase-magnitude optimization with peak local SAR constraints using VOPs. Given the great similarities in the image quality when using the localized and nonlocalized AMORE designs, the latter appears to be a promising and clinically feasible solution for torso imaging at UHF that also helps simplify the

pTx workflow by reducing the need to define a local target while improving overall imaging quality.

6 | CONCLUSION

In this study, we demonstrated improved TSE images in multiple anatomies when using the proposed nonlocalized efficiency shimming and its extension AMORE at UHF. Observed improvements included reduced signal dropout and higher transmit B_1^+ efficiency when compared to previously proposed approaches. The nonlocalized efficiency shimming is a simple and robust approach to improve image uniformity in smaller targets such as brain and knee, whereas AMORE may serve as a clinically feasible routine for TSE acquisitions with larger FOVs such as needed in the human torso.

ACKNOWLEDGMENT

The authors would like to thank Maria Giovanna Di Trani for helping with the acronym of the proposed method, and Edward J. Auerbach for tips on sequence programming.

FUNDING INFORMATION

Supported by the National Institutes of Health (NIH), National Institute of Biomedical Imaging and Bioengineering (NIBIB) grants P41 EB027061 and R01 EB029985

ORCID

Xiaoxuan He https://orcid.org/0000-0003-0885-912X
Simon Schmidt https://orcid.org/0000-0003-1835-4002
Steen Moeller https://orcid.org/0000-0003-1698-7260
Gregory J. Metzger https://orcid.org/0000-0002-3187-6529

REFERENCES

1. Guerin B, Villena JF, Polimeridis AG, et al. The ultimate signal-to-noise ratio in realistic body models. *Magn Reson Med*. 2017;78:1969-1980.
2. Budde J, Shajan G, Hoffmann J, Ugurbil K, Pohmann R. Human imaging at 9.4 T using T-2*-, phase-, and susceptibility-weighted contrast. *Magn Reson Med*. 2011;65:544-550.
3. Katscher U, Bornert P, Leussler C, van den Brink JS. Transmit SENSE. *Magn Reson Med*. 2003;49:144-150.
4. Zhu Y. Parallel excitation with an array of transmit coils. *Magn Reson Med*. 2004;51:775-784.
5. Saekho S, Yip CY, Noll DC, Boada FE, Stenger VA. Fast-kz three-dimensional tailored radiofrequency pulse for reduced B1 inhomogeneity. *Magn Reson Med*. 2006;55:719-724.
6. Cloos MA, Boulant N, Luong M, et al. kT-points: short three-dimensional tailored RF pulses for flip-angle homogenization over an extended volume. *Magn Reson Med*. 2012;67:72-80.
7. Grissom W, Yip CY, Zhang Z, Stenger VA, Fessler JA, Noll DC. Spatial domain method for the design of RF pulses in multicoil parallel excitation. *Magn Reson Med*. 2006;56:620-629.
8. Adriany G, Van de Moortele PF, Wiesinger F, et al. Transmit and receive transmission line arrays for 7 Tesla parallel imaging. *Magn Reson Med*. 2005;53:434-445.
9. Mao W, Smith MB, Collins CM. Exploring the limits of RF shimming for high-field MRI of the human head. *Magn Reson Med*. 2006;56:918-922.
10. Metzger GJ, Snyder C, Akgun C, Vaughan T, Ugurbil K, Van de Moortele PF. Local B1+ shimming for prostate imaging with transceiver arrays at 7T based on subject-dependent transmit phase measurements. *Magn Reson Med*. 2008;59:396-409.
11. Erturk MA, Li X, Van de Moortele PF, Ugurbil K, Metzger GJ. Evolution of UHF body imaging in the human torso at 7T: technology, applications, and future directions. *Top Magn Reson Imaging*. 2019;28:101-124.
12. Ugurbil K, Van de Moortele PF, Grant A, et al. Progress in imaging the human torso at the ultrahigh fields of 7 and 10.5 T. *Magn Reson Imaging Clin N Am*. 2021;29:E1-E19.
13. Metzger GJ, van de Moortele PF, Akgun C, et al. Performance of external and internal coil configurations for prostate investigations at 7 T. *Magn Reson Med*. 2010;64:1625-1639.
14. Metzger GJ, Auerbach EJ, Akgun C, et al. Dynamically applied B1+ shimming solutions for non-contrast enhanced renal angiography at 7.0 Tesla. *Magn Reson Med*. 2013;69:114-126.
15. Orzada S, Maderwald S, Poser BA, Bitz AK, Quick HH, Ladd ME. RF excitation using time interleaved acquisition of modes (TIAMO) to address B1 inhomogeneity in high-field MRI. *Magn Reson Med*. 2010;64:327-333.
16. Griswold MA, Jakob PM, Heidemann RM, et al. Generalized autocalibrating partially parallel acquisitions (GRAPPA). *Magn Reson Med*. 2002;47:1202-1210.
17. Orzada S, Maderwald S, Poser BA, et al. Time-interleaved acquisition of modes: an analysis of SAR and image contrast implications. *Magn Reson Med*. 2012;67:1033-1041.
18. Brunheim S, Gratz M, Johst S, et al. Fast and accurate multi-channel B1+ mapping based on the TIAMO technique for 7T UHF body MRI. *Magn Reson Med*. 2018;79:2652-2664.
19. Liebert A, Zaiss M, Gumbrecht R, et al. Multiple interleaved mode saturation (MIMOSA) for B1 (+) inhomogeneity mitigation in chemical exchange saturation transfer. *Magn Reson Med*. 2019;82:693-705.
20. Van de Moortele PF, Akgun C, Adriany G, et al. B(1) destructive interferences and spatial phase patterns at 7 T with a head transceiver array coil. *Magn Reson Med*. 2005;54:1503-1518.
21. Zhu Y, Deniz C, Alon L, Fautz H, Sodickson D. Undestanding Parallel Transmit Array Efficiency. In Proceedings of the 18th Annual Meeting of ISMRM, Stockholm, Sweden, 2010. p. 1518.
22. Deniz CM, Brown R, Lattanzi R, Alon L, Sodickson DK, Zhu Y. Maximum efficiency radiofrequency shimming: theory and initial application for hip imaging at 7 Tesla. *Magn Reson Med*. 2013;69:1379-1388.
23. Setsompop K, Wald L, Adalsteinsson E. In Proceedings of the 15th Annual Meeting of ISMRM, Berlin, Germany, 2007. p. 1687.
24. Eichfelder G, Gebhardt M. Local specific absorption rate control for parallel transmission by virtual observation points. *Magn Reson Med*. 2011;66:1468-1476.

25. Chung S, Kim D, Breton E, Axel L. Rapid B-1(+) mapping using a preconditioning RF pulse with TurboFLASH readout. *Magn Reson Med*. 2010;64:439-446.
26. Goerke U, Bolan P, Akgun C, et al. Ultrahigh magnetic field imaging of the knee using a transmit/receive array coil. In Proceedings of the 16th Annual Meeting of ISMRM, Toronto, Ontario, Canada, 2008. p. 744.
27. Erturk MA, Raaijmakers AJ, Adriany G, Ugurbil K, Metzger GJ. A 16-channel combined loop-dipole transceiver array for 7 Tesla body MRI. *Magn Reson Med*. 2017;77:884-894.
28. Hennig J, Weigel M, Scheffler K. Multiecho sequences with variable refocusing flip angles: optimization of signal behavior using smooth transitions between pseudo steady states (TRAPS). *Magn Reson Med*. 2003;49:527-535.
29. Mugler JP 3rd. Optimized three-dimensional fast-spin-echo MRI. *J Magn Reson Imaging*. 2014;39:745-767.
30. Steensma BR, Voogt IJ, Leiner T, et al. An 8-channel Tx/Rx dipole array combined with 16 Rx loops for high-resolution functional cardiac imaging at 7 T. *MAGMA*. 2018;31:7-18.
31. Rietsch SHG, Orzada S, Maderwald S, et al. 7T ultra-high field body MR imaging with an 8-channel transmit/32-channel receive radiofrequency coil array. *Med Phys*. 2018;45:2978-2990.
32. Uecker M, Lai P, Murphy MJ, et al. ESPIRiT--an eigenvalue approach to autocalibrating parallel MRI: where SENSE meets GRAPPA. *Magn Reson Med*. 2014;71:990-1001.
33. Akcakaya M, Moeller S, Weingartner S, Ugurbil K. Scan-specific robust artificial-neural-networks for k-space interpolation (RAKI) reconstruction: database-free deep learning for fast imaging. *Magn Reson Med*. 2019;81:439-453.
34. Hammernik K, Klatzer T, Kobler E, et al. Learning a variational network for reconstruction of accelerated MRI data. *Magn Reson Med*. 2018;79:3055-3071.
35. Han Y, Sunwoo L, Ye JC. K -space deep learning for accelerated MRI. *IEEE Trans Med Imaging*. 2020;39:377-386.
36. Hyun CM, Kim HP, Lee SM, Lee S, Seo JK. Deep learning for undersampled MRI reconstruction. *Phys Med Biol*. 2018;63:135007.
37. Yaman B, Hosseini SAH, Moeller S, Ellermann J, Ugurbil K, Akcakya M. Self-supervised physics-based deep learning MRI reconstruction without fully-sampled data. 2020 IEEE 17th International Symposium on Biomedical Imaging (ISBI), 2020. p. 921–925.
38. Zhu B, Liu JZ, Cauley SF, Rosen BR, Rosen MS. Image reconstruction by domain-transform manifold learning. *Nature*. 2018;555:487-492.
39. Tustison NJ, Avants BB, Cook PA, et al. N4ITK: improved N3 bias correction. *IEEE Trans Med Imaging*. 2010;29:1310-1320.
40. Chebrolu VV, Kollasch PD, Deshpande V, et al. Uniform combined reconstruction of multichannel 7T knee MRI receive coil data without the use of a reference scan. *J Magn Reson Imaging*. 2019;50:1534-1544.
41. Erturk MA, Wu X, Eryaman Y, et al. Toward imaging the body at 10.5 Tesla. *Magn Reson Med*. 2017;77:434-443.
42. Sadeghi-Tarakameh A, DelaBarre L, Lagore RL, et al. In vivo human head MRI at 10.5T: a radiofrequency safety study and preliminary imaging results. *Magn Reson Med*. 2020;84:484-496.
43. He X, Erturk MA, Grant A, et al. First in-vivo human imaging at 10.5T: imaging the body at 447 MHz. *Magn Reson Med*. 2020;84:289-303.

SUPPORTING INFORMATION

Additional supporting information may be found in the online version of the article at the publisher's website.

FIGURE S1. Comparisons of the default CP mode and the proposed non-localized efficiency shim in the knee imaging study illustrated by the histograms of voxel-wise B_1^+ (A, D), predicted sagittal B_1^+ maps (B, E), and sagittal TSE images (C, F). Both the default CP mode and the proposed shim used the same transmitter voltage for data acquisition. Compared with the default CP mode, the proposed shim increased both minimum and overall B_1^+, reduced areas of low B_1^+ and reduced signal dropout (lower right corner). μ: mean value (red solid line); RMS: root mean square (red dashed line).

FIGURE S2. In-vivo T2w TSE images acquired in 4 subjects using local RF shimming, LS-TIAMO and AMORE (both with non-localized and localized approaches). Overall, AMORE significantly reduced B1+ nulls in the interior of the torso while maintaining near ideal contrast in the prostate compared with the locally shimmed acquisition, at a mild cost of over-flipping in the subcutaneous lipid near the transmit elements of the closely fitting RF coil.

How to cite this article: He X, Schmidt S, Zbýň Š, Haluptzok T, Moeller S, Metzger GJ. Improved TSE imaging at ultrahigh field using nonlocalized efficiency RF shimming and acquisition modes optimized for refocused echoes (AMORE). *Magn Reson Med*. 2022;88:1702-1719. doi: 10.1002/mrm.29318

APPENDIX A

Here we demonstrate by numerical analyses how previously derived small tip angle formulation for TIAMO can be generalized to TSE based acquisitions. The equation of the observable MRI signal $S(\boldsymbol{r})$ can be written as:

$$S(\boldsymbol{r}) \propto B_1^-(\boldsymbol{r}) \cdot W(\boldsymbol{r}) \cdot f\left(\boldsymbol{\theta}(\boldsymbol{r}), \mathrm{B}_1^+(\boldsymbol{r})\right)$$

where $B_1^-(\boldsymbol{r})$ is the receive sensitivity, $W(\boldsymbol{r})$ is proton density weighting, $f\left(\boldsymbol{\theta}(\boldsymbol{r}), \mathrm{B}_1^+(\boldsymbol{r})\right)$ is the steady state signal of the magnetization as dictated by relaxometry parameter set $\boldsymbol{\theta}(\boldsymbol{r})$, transmit field $B_1^+(\boldsymbol{r})$ and underlying acquisition sequence. Note that for simplicity the spatial encoding phase term is ignored. For TSE acquisitions, the k-space lines are acquired at different effective echo times.

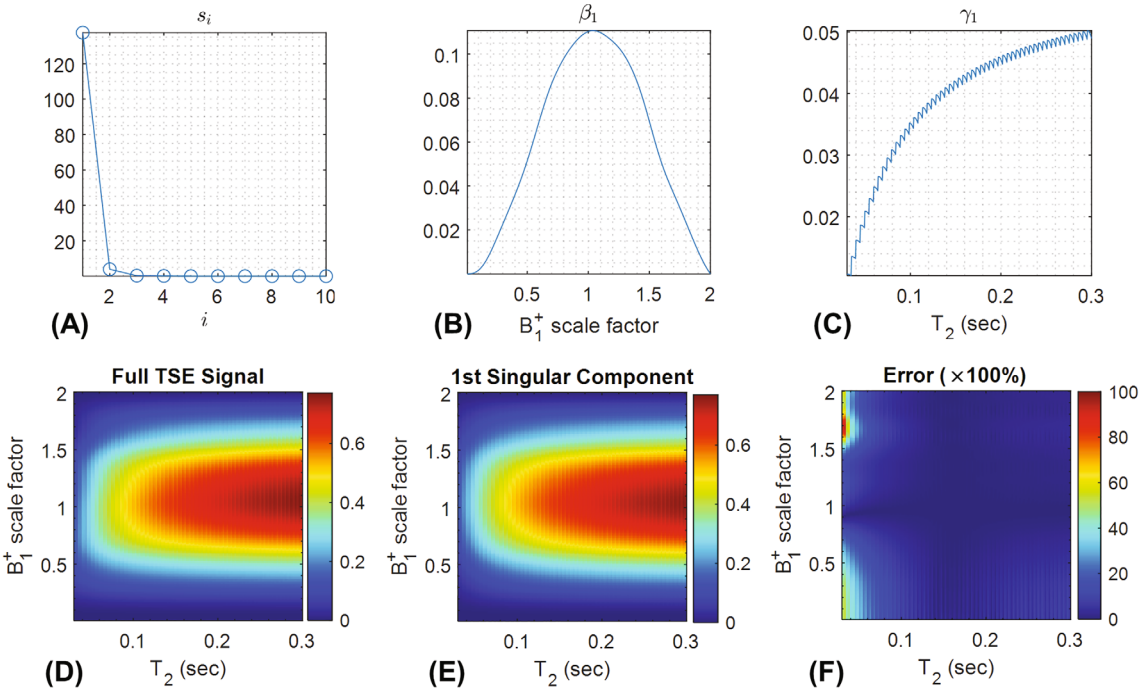

FIGURE 9 Demonstration of the low-rank approximation of the TSE signal simulated with the following parameters: TR/TE 7000/62 ms, excitation/refocusing flip angle 90/120°, turbo factor 13, echo spacing 8.82 ms, T_1 ranges from 1000 to 2000 ms in increments of 100 ms, T_2 ranges from 30 to 300 ms in increments of 5 ms, $B_1{}^+$ scale factor ranges from 0.01 to 2 in increments of 0.01. The 10 largest singular values are plotted in (A). The magnitude of the left and right singular vector β_1, γ_1 are shown in (B) and (C), respectively. Note that β_1 is dominated by $B_1{}^+$, whereas γ_1 is dominated by T_2. The slight oscillations on the curve in (C) are due to T_1 relaxation over the ranges of simulated values. The TSE signal can be well approximated by the largest singular component alone (i.e., $s_1 \cdot \beta_1 \cdot \gamma_1^H$), as shown in (D, E). The approximation error is most notable for very short T_2 with a significant underflipping or overflipping as shown in (F)

However, the imaging protocol is typically optimized to maintain T_2 weighting by using longer repetition times (TR > 3*T_1), appropriate turbo factors and k-space ordering. Therefore, it can be assumed in general that the contrast in TSE is dominated by the central k-space lines to simplify analysis.

To generalize TIAMO, the remaining question is whether the nonlinear term $f\left(\boldsymbol{\theta}(\boldsymbol{r}), \mathrm{B}_1^+(\boldsymbol{r})\right)$ can be decomposed into a multiplicative form in a similar way as the small tip angle approximation. This can be investigated by performing a singular value decomposition on the dictionary of signals generated by simulating the imaging sequence with a range of $B_1{}^+$ and relaxometry parameters that cover the typical values encountered in experiments. Empirically, we observe that $f\left(\boldsymbol{\theta}(\boldsymbol{r}), \mathrm{B}_1^+(\boldsymbol{r})\right)$ is low-rank and can therefore be approximated by:

$$f\left(\boldsymbol{\theta}(\boldsymbol{r}), \mathrm{B}_1^+(\boldsymbol{r})\right) \approx \sum_{k=1}^{N_k} s_k \cdot \beta_k(\boldsymbol{r}) \cdot \gamma_k^H(\boldsymbol{r})$$

in which s_k is the k-th of the N_k largest singular value, $\beta_k(\boldsymbol{r})$ and $\gamma_k(\boldsymbol{r})$ are the k-th left and right singular vectors, respectively. For T_2 and PD weighted TSE acquisitions, $f\left(\boldsymbol{\theta}(\boldsymbol{r}), \mathrm{B}_1^+(\boldsymbol{r})\right)$ can be well approximated by the largest singular value and its corresponding singular vectors alone (i.e., $N_k = 1$) except for very short T_2 with significant under-flipping or over-flipping (Figure 9). Therefore, the signal equation can be approximated by:

$$\begin{aligned} S(\boldsymbol{r}) &\propto B_1^-(\boldsymbol{r}) \cdot W(\boldsymbol{r}) \cdot f\left(\boldsymbol{\theta}(\boldsymbol{r}), \mathrm{B}_1^+(\boldsymbol{r})\right) \\ &\approx B_1^-(\boldsymbol{r}) \cdot W(\boldsymbol{r}) \cdot s_1 \cdot \beta_1(\boldsymbol{r}) \cdot \gamma_1^H(\boldsymbol{r}) \end{aligned}$$

$\beta_1(\boldsymbol{r})$ is observed to be mostly dominated by $B_1{}^+$ whereas $\gamma_1(\boldsymbol{r})$ is mostly dominated by T_2. Like the original small tip angle formulation used in TIAMO, $\beta_1(\boldsymbol{r})$ appears as virtual receive sensitivity and $s_1 \cdot \gamma_1^H(\boldsymbol{r})$ is the underlying T_2 weighted component. The analysis here validates the observation in the initial TIAMO work that TIAMO works well for TSE acquisitions even though it is derived from the small tip angle approximation.

When images acquired with different $B_1{}^+$ modes are combined using sum of squares, the final image contrast will be determined by the signal from each mode. To get the optimal T2w contrast, the ideal combination of modes will be a high $B_1{}^+$ (i.e., calibrated) with a low $B_1{}^+$, where the former is expected to provide a correct and dominating contrast in the combined image. The sub-optimal combination of modes will be a high $B_1{}^+$ with a medium $B_1{}^+$,

where the final combined contrast may get biased if the latter mode produces a sub-optimal T2w contrast such as for very short T_2 tissues. The worst combination of modes will be a medium/low B1+ and a medium/low B_1^+, where neither mode provides a correct T2w contrast for the combined image. Therefore, to maintain the T2w contrast in the TIAMO image, it is necessary that at least 1 of the modes achieves the desired flip angle, analogous to designing a physical receiver array that has at least 1 of the coil elements to cover any given region in the imaging FOV.